Imaging inflammation in mouse colon using a rapid stage-scanning confocal fluorescence microscope

Meagan A. Saldua
Cory A. Olsovsky
Evelyn S. Callaway
Robert S. Chapkin
Kristen C. Maitland

Imaging inflammation in mouse colon using a rapid stage-scanning confocal fluorescence microscope

Meagan A. Saldua,[a] Cory A. Olsovsky,[a] Evelyn S. Callaway,[b] Robert S. Chapkin,[b] and Kristen C. Maitland[a]
[a]Texas A&M University, Department of Biomedical Engineering, 3120 TAMU, College Station, Texas, 77843-3120
[b]Texas A&M University, Program in Integrative Nutrition & Complex Diseases, 2253 TAMU, College Station, Texas 77843-2253

Abstract. Large area confocal microscopy may provide fast, high-resolution image acquisition for evaluation of tissue in pre-clinical studies with reduced tissue processing in comparison to histology. We present a rapid beam and stage-scanning confocal fluorescence microscope to image cellular and tissue features along the length of the entire excised mouse colon. The beam is scanned at $8,333$ lines/sec by a polygon scanning mirror while the specimen is scanned in the orthogonal axis by a motorized translation stage with a maximum speed of 7 mm/sec. A single $1 \times 60 \text{ mm}^2$ field of view image spanning the length of the mouse colon is acquired in 10 s. Z-projection images generated from axial image stacks allow high resolution imaging of the surface of non-flat specimens. In contrast to the uniform size, shape, and distribution of colon crypts in confocal images of normal colon, confocal images of chronic bowel inflammation exhibit heterogeneous tissue structure with localized severe crypt distortion. © *2012 Society of Photo-Optical Instrumentation Engineers (SPIE).* [DOI: 10.1117/1.JBO.17.1.016006]

Keywords: Confocal microscopy; stage scanning; large area microscopy; chronic inflammation; inflammatory bowel disease.

Paper 11438 received Aug. 15, 2011; revised manuscript received Nov. 10, 2011; accepted for publication Nov. 14, 2011; published online Feb. 8, 2012.

1 Introduction

1.1 Bowel Inflammation

Autoimmune and chronic inflammatory diseases are a global health problem. With respect to the burden of inflammatory bowel diseases (IBD), approximately 1.5 million Americans exhibit chronic debilitating inflammatory conditions of the intestinal tract, leading to distressing symptoms and an impaired quality of life (with an estimated annual cost exceeding $2 billion).[1] Patients experiencing IBD often report symptoms such as abdominal pain, diarrhea, rectal bleeding, weight loss, fever, and fatigue. Ulcerative colitis and Crohn's disease are two distinct forms of IBD.[2] In ulcerative colitis, inflammation is typically restricted to the mucosa in the colon. In Crohn's disease, any area within the entire gastrointestinal tract may be susceptible to inflammation.

One in 19 Americans are at risk of developing colorectal cancer in their lifetime. Detection and removal of precancerous polyps has reduced the incidence and mortality of this disease.[3] Patients with IBD have an increased risk for developing colorectal cancer; after seven years of inflammation, the risk of developing cancer increases by 0.5 to 1% every year.[4] Although studies have shown this direct relationship between inflammation and colon cancer, early cancer detection remains a challenge, even for this high-risk population.[5] Currently, high-risk patients are recommended to begin colonoscopy cancer screening at an earlier age than healthy adults.[6]

Epidemiologic studies have shown that diet is also a major risk factor for colorectal cancer.[3] For example, high consumption of red or processed meats increases the risk of colorectal cancer by 28% and 20%, respectively.[7,8] Recent studies indicate that bioactive food components containing n-3 polyunsaturated fatty acids (PUFA) may have antitumorigenic effects by reducing inflammation in an animal model of colitis-associated cancer.[9,10] Data has revealed a "protective effect" of n-3 PUFA (fish oil) on colon cancer and in contrast, n-6 PUFA (vegetable oil) has been shown to amplify the formation of colon tumors. This may suggest that IBD patients could moderate cancer development by modifying their diet.[11]

Colon crypt and tissue structural changes in pre-clinical studies are typically characterized using histopathology. Histology provides images of cellular and tissue structure after animal sacrifice, colon removal, and washing and staining of the tissue. This is a time-sensitive process that can introduce artifacts during tissue preparation. In histological images of normal colon tissue, the cylindrical crypt openings are aligned parallel to one another and exhibit a uniform hexagonal pattern when observed from an *en face* view.[12] This pattern is characteristic of normal colonic tissue with only slight variation in colon size and arrangement. Inflamed tissue varies in morphological structure compared to normal colon tissue. Crypt structure may be lost, and tissue architecture is replaced by a disordered crypt arrangement with heterogeneous crypt size and shape, which can be seen both in histology and confocal endomicroscopy.[13,14] Due to the heterogeneity of inflamed tissue, examination of a small tissue sample by histology may not be indicative of the most severe disease state elsewhere in the colon. The 'swiss roll' technique may be used to visualize histological features along the length of the colon, but provides only a thin section through the tissue.[15] With transition from inflammation to neoplasia, dysplasia or cancer can affect any part of the colon with various magnitudes at different locations, complicating

Address all correspondence to: Kristen C. Maitland, Texas A&M University, Department of Biomedical Engineering, 5045 Emerging Technologies Bldg, 3120 TAMU, College Station, Texas 77843. Fax: (979) 845–4450; E-mail: kmaitland@tamu.edu.

localization and characterization of disease by histopathology in pre-clinical studies.[5]

Rapid imaging of bulk tissue along the length of freshly excised colon could provide sufficient information on crypt structure throughout the colon to characterize tissue in pre-clinical studies. Reduced tissue processing, fast image acquisition, and evaluation over a larger field could increase throughput and quantification in pre-clinical studies of IBD. Our custom-designed confocal microscope can achieve a single $1 \times 60 \, mm^2$ field of view image in 10 s. Compared to other confocal imaging systems, this system is capable of producing large area images in a short period of time. Here, we present stage-scanning confocal microscopy as a technique to rapidly image the length of the colon with minimal tissue processing.

1.2 Confocal Microscopy

Confocal microscopy can provide high resolution images of bulk tissue with minimal tissue processing and fast image acquisition. In contrast to the physical sectioning and two-dimensional imaging of traditional histology, confocal imaging allows "optical sectioning" of bulk tissue, enabling acquisition of three dimensional images of intact tissue.[16,17] This technique has been translated to the clinical setting where *in vivo* confocal microendoscopy is currently being explored for guiding biopsy in the gastrointestinal tract.[18] However, even with mosaicing to expand the imaging field, field of view (FOV) still remains limited.

The high resolution of confocal microscopy is achieved by placing a pinhole in front of the detector in a conjugate image plane of the focal spot in the sample. Out-of-focus light is significantly rejected by the pinhole. Two-and three-dimensional images can be generated by scanning the beam or the sample.[19–21] Although historically, stage-scanning has been used quite extensively,[22] the speed of translation stages has limited the speed of image acquisition. Modern confocal microscopes typically use some form of beamscanning to maximize image acquisition speed,[23] but the FOV is typically limited to less than $500 \times 500 \, \mu m^2$.[24] A larger FOV can be achieved by stitching images together using a mosaicing technique.[25]

FOV and image acquisition speed can be increased by combining beam and stage scanning. Recently, beam and stage scanning used with mosaicing has been implemented to increase acquisition speed of large FOV reflectance confocal images for dermatological applications.[26] A $10 \times 10 \, mm^2$ strip mosaic was acquired in 3 min. Similarly, spectral encoding in one axis to scan 180 μm and stage scanning in both lateral axes with mosaicing has been used to image large esophageal biopsy specimens.[27] Axial scanning of the objective lens using a piezoelectric transducer allowed three-dimensional images over a 120 to 150 μm depth range. Fields of view ranging from $2 \times 1 \, mm^2$ to $5 \times 3.6 \, mm^2$ were acquired in 2.5 to 15 minutes. Large FOV fluorescence confocal imaging of the mouse colon and other organs *in vivo* through a gradient index (GRIN) side-viewing microprobe was recently achieved by versatile multidimensional scanning.[28] The $250 \times 250 \, \mu m^2$ raster-scanned FOV is extended by mosaicing frames captured at 30 frames per second while rotationally scanning the microprobe and/or translating the sample or animal to scan along the length of a lumen. The focal depth position in the sample is adjusted by altering the focal position at the proximal face of the GRIN relay lens. 60,000 frames acquired in over 30 minutes from a 12 mm length of mouse colon after intravenous injection of fluorescent dye

are reconstructed into beautiful images of the vasculature in two and three dimensions and with multiple scales.

We exploit a polygon mirror beam scanner and a fast motorized translation stage to rapidly acquire confocal images with an extended FOV in one axis. We have acquired a single high aspect ratio, 60-megapixel, $1 \times 60 \, mm^2$ image in 10 s, extending image size in one axis and increasing acquisition speed over previously reported systems. Translation of the sample in the third dimension allows three-dimensional imaging and two-dimensional projections of tissue to accommodate specimens with an uneven surface. This high aspect ratio imaging is ideal for imaging tissue structure along the gastrointestinal tract. We present the use of combined beam and stage scanning in confocal microscopy to extend the FOV to image and evaluate freshly excised mouse colon to provide qualitative information on crypt structure along the length of the colon.

2 Materials and Methods

2.1 System Design

Figure 1 shows a schematic of the constructed confocal fluorescence microscope [Fig. 1(a)] and a photo of the current setup [Fig. 1(b)]. The upright confocal microscope has a 40 mW, 488 nm, continuous wave, externally doubled diode laser (Excelsior, Spectra-Physics, Santa Clara, CA) for fluorescence imaging. The laser beam passes through a spatial filter, which also serves as a beam expander, and reflects off of a dichroic mirror (z488rdc, Chroma Technology Corporation, Rockingham, VT). A custom-designed polygon scanner (Lincoln Laser, Phoenix, AZ) with a scan rate of 2.5 to 8.75 kHz serves as the line scan, and a galvanometer scanner (6220H M40B, Cambridge Technology, Lexington, MA) with a scan rate up to 15 frames per second (fps) provides the frame scan for image acquisition in traditional raster-scanning mode, producing "square" two-dimensional images. Two telescopes are used to image both mirrors onto the back aperture of the 40×, 0.8-numerical aperture, 3.5 mm working distance water immersion microscope objective lens (MRD07420, Nikon). The sample is positioned on an XYZ-motorized stage (KT-LSM100A, Zaber Technologies Inc, Vancouver, British Columbia, Canada) with 0.05 μm resolution, 100 mm of travel in each axis, and 7 mm/sec maximum speed. Fluorescence is excited in the sample, collected by the objective, passed back through the telescope system, and descanned by the scanning mirrors. After passing through the dichroic mirror to the detection
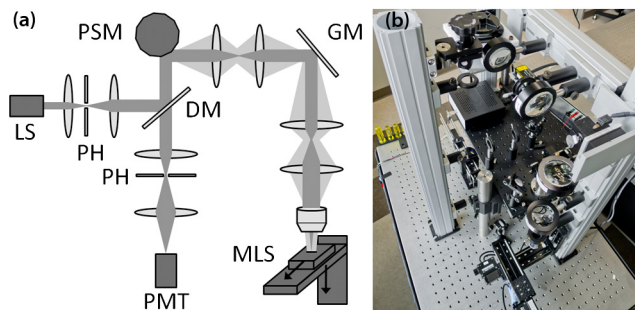
Fig. 1 Confocal fluorescence microscope schematic (a) and photograph of the system (b). LS: laser source, PH: pinhole, DM: dichroic mirror, PSM: polygon scanning mirror, GM: galvanometer scanning mirror, MLS: motorized linear stage, PMT: photomultiplier tube.

arm, the signal is focused onto the confocal detection pinhole and then refocused onto a photomultiplier tube (PMT) detector (H9433-03MOD, Hamamatsu, Bridgewater, NJ) with gain set to 10^4 and frequency bandwidth of 10 MHz. A frame grabber (NI PCI-1410, National Instruments, Austin, TX) digitizes the PMT signal with a 29 MHz pixel clock and generates images. Both of the scanning mirrors and the stage are controlled by LabVIEW software (National Instruments), and the mirrors are driven by a data acquisition (DAQ) board (NI PCI-6251, National Instruments).

To maximize signal throughput and maintain sufficient axial sectioning, the size of the detection pinhole was selected to be approximately equal to the projected Airy disk. The intensity distribution as a function of normalized radial optical coordinate, v, for a single fluorescent point object in focus is given by

$$I(\nu) = \left\{ 4 \left[\frac{J_1(\nu)}{\nu} \cdot \frac{J_1(\nu/\beta)}{\nu/\beta} \right] \right\}^2, \quad (1)$$

where J_1 is a first-order Bessel function of the first kind and β is the ratio of the emission wavelength to excitation wavelength.[29] The first minimum of the lateral response in Eq. (1) occurs at $v_o = 3.83$. Using

$$d = \frac{\nu_o}{\pi} \lambda_{\text{ex}} \frac{M}{NA}, \quad (2)$$

the diameter of the projected central disk can be calculated to be 9.9 μm for our system with excitation wavelength $\lambda_{\text{ex}} = 488$ nm, total system magnification $M = 13.33$, and objective lens numerical aperture $NA = 0.8$. Therefore, a 10 μm diameter pinhole was used in the confocal detection spatial filter, corresponding to a normalized pinhole radius $v_p = 3.86$. The theoretical lateral resolution as defined by the Rayleigh criterion can be calculated by converting the normalized pinhole radius to real radial distance in the object, $r = 0.375$ μm. To evaluate the optical sectioning capability, we use the plot of the half-width, $u_{1/2}$, of the axial response of a planar fluorescent object translated through the focus as a function of v_p and β.[29] For $v_p = 3.86$ and $\beta = 1.08$, the normalized half-width of the axial point spread function is $u_{1/2} = 5.6$. Converting to the half-width half maximum in spatial dimensions using

$$z_{1/2} = u_{1/2} \frac{\lambda}{2\pi} \cdot \frac{n}{NA^2}, \quad (3)$$

yields a full width half maximum (FWHM) axial resolution of 1.8 μm.

The scanning microscope can be operated in two modes: raster-scanning or stage-scanning. In either mode, the polygon scanner provides the fast axis scan, or line scan, at a scan rate of 8.33 kHz. In raster-scanning mode, the slow axis scan, or frame scan, is provided by the galvanometer scanning mirror, generating 1×1 mm^2 FOV images at 8 frames per second. In stage-scanning mode, the galvanometer scanning mirror is positioned in the center of its scan range (center of FOV), and the motorized linear stage translates the sample in the second axis. The image acquisition speed, FOV, and digital image size are limited by the stage speed, stage travel range, and frame grabber memory, respectively. Acquisition of a single 60 megapixel image of 1×60 mm^2 FOV takes approximately 10 s. Acquisition of a stack of 60 frames with a 1×60 mm^2 FOV and a 10 μm

axial step interval between consecutive images over an axial range of 600 μm takes approximately 20 min. The 600 μm axial range was necessary to capture the topography of the sample and to accommodate a minor incline of the translation stage over the 100 mm of travel. The XYZ motorized translation stage has three independently mounted axes; re-positioning the stage may reduce the required axial range and, consequently, increase the three-dimensional image acquisition rate.

To increase FOV and data acquisition speed, lateral resolution is sacrificed by under-sampling with a 1 μm pixel size, which is significantly larger than the 0.375 μm theoretical lateral resolution. The system lateral resolution was measured by capturing an image of a reflective Ronchi grating (Edmund Optics) with 40 line pairs/mm. A line profile was plotted across several grating edges. The distance between the 10% and 90% intensity values was recorded for five edges and then averaged. The measured lateral resolution is approximately 1 μm. For our application, imaging tissue and crypt structure in the mouse colon, lateral resolution is less important than the field of view, speed of image acquisition, and file size. We can resolve 2 μm according to the Nyquist Theorem; therefore, the sampling is sufficient to resolve individual cell nuclei, which are approximately 5 to 10 μm in diameter, and crypt lumen, ranging from 40 to 70 μm in diameter in normal mouse colon tissue. To measure axial resolution, a reflective silver mirror was translated through the focal plane. Intensity values were recorded from the PMT and plotted. The measured full width half maximum axial resolution is less than 2 μm. Table 1 summarizes the imaging parameters for the confocal fluorescence microscope system in raster-scanning and stage-scanning modes.

2.2 Sample Preparation and Imaging

Human colitis can be modeled in healthy rodents by treatment with dextran sodium sulfate (DSS) added to their drinking water.[30] An increase in disease duration results in an increased rate of neoplastic development. When used in conjunction with

Table 1 List of system and imaging parameters for the confocal fluorescence microscope.

System/Imaging parameters	
Excitation wavelength	488 nm
Detection wavelength	>495 nm
Lateral resolution	1 μm
Axial resolution	2 μm
Line scan speed	8333 lines/sec
Raster-scanning mode	
Field of view	1 mm × 1 mm
Frame scan speed	8 frames/sec
Stage-scanning mode	
Field of view	1 mm × ≤ 60 mm
Frame scan speed	7 mm/sec

azoxymethane (a colon-specific carcinogen), the mice can develop colon cancer.[31]

Black C57BL/6 mice were used for this study. The animal protocol was reviewed and approved by the Texas A&M University Institutional Animal Care and Use Committee. To induce chronic inflammation, a mouse was treated with 2.5% DSS (MP Biomedicals) for five days followed by a 17-day recovery period. On day 22, the treatment and recovery periods were repeated. Finally, the mouse was treated with 2% DSS for four days. Termination occurred on day 57.

Following colon resection, the normal and inflamed mouse colons were opened longitudinally along a fatty tissue line. The tissue was rinsed in two phosphate buffered solution (PBS) washes to remove any fecal matter. The colons were stained with 1 mg/mL of acridine orange (Sigma-Aldrich) for two minutes and then rinsed in PBS for one minute. Each mouse colon was placed flat in a Petri dish with the inside of the colon facing up. A microscope slide was placed on top of the colon to flatten and immobilize the tissue during imaging.

When imaging a mouse colon, the tissue is positioned in the focal plane of the microscope using raster-scanning mode. In order to evaluate tissue features along the length of the colon, extended FOV confocal images are acquired using stage-scanning mode. The long axis of the FOV is specified based on the length of the mouse colon. The topography of a mouse colon varies along its length; therefore it was necessary to acquire vertical stacks of extended confocal images to capture information at different focal planes. The number of images in a stack or the depth of imaging is determined by the topography and the penetration of light into the tissue. The long stacks were used to build a Z-projection image that reconstructs the surface profile of the mouse colon tissue while maintaining high resolution features. For the images presented in this paper, 70 extended confocal images, approximately 1×56 mm^2, of normal mouse colon tissue and 50 images, approximately 1×60 mm^2, of

chronic inflamed colon were acquired with a 10 μm step interval between consecutive frames in the axial direction.

Following confocal imaging, tissue samples from proximal, middle, and distal regions of the colon were prepared for histological processing. In contrast to the standard transverse slicing, the tissue was oriented to generate tissue slices parallel to the surface of the tissue to enable a comparison to the *en face* confocal images. The tissue sections were stained with hematoxylin and eosin (H&E).

2.3 Image Analysis

Images stacks were processed into two-dimensional projections and videos using Photoshop (Adobe Systems Inc., San Jose, CA) and ImageJ (National Institutes of Health, http://rsbweb .nih.gov/ij). Each image stack was reduced to a two-dimensional maximum intensity Z-projection image. The maximum intensity projection command in ImageJ selects the maximum pixel value for a single pixel location within a stack of images and generates an image using the maximum values for all pixel locations. Because the colon tissue topography varies significantly within this large field of view and confocal sectioning yields a thin optical slice through the tissue, the Z-projection allows visualization of the colon crypts near the surface along the length of the colon. It was determined that the image quality of Z-projections was improved by using every other image in the stack, resulting in 20 μm axial separation between images in the stack. Figure 2 demonstrates the maximum intensity Z-projection and three dimensional reconstruction for a stack of confocal images. Figures 2(a)–2(d) show four confocal images of a 1×2 mm^2 region separated by 20 μm in depth taken from the image stack. Figure 2(e) is a zoomed-in section depicted by the white box in Fig. 2(a) exhibiting bright nuclei surrounding colon crypts. The corresponding maximum intensity Z-projection is shown in Fig. 2(f) to demonstrate the effect of the projection
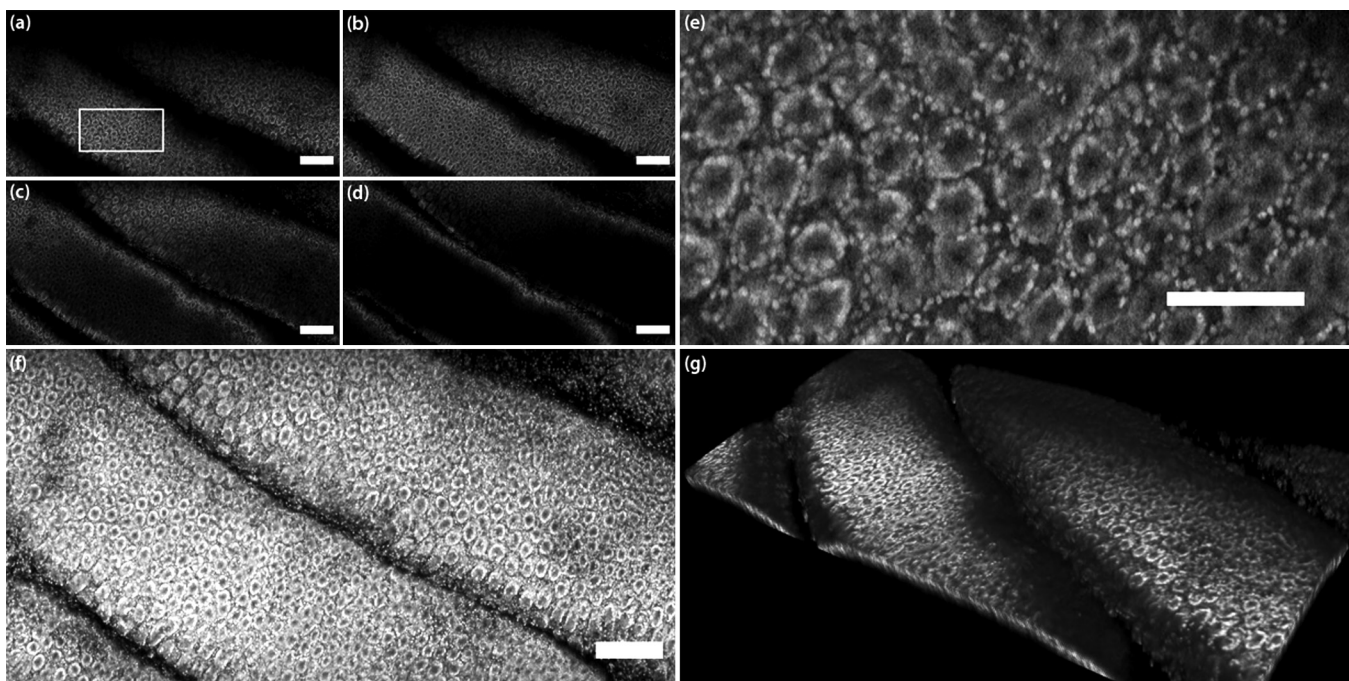
Fig. 2 Selected confocal frames from an image stack for a single region, 1×2 mm^2 FOV, obtained (a) near the surface and (b) 20 μm, (c) 40 μm, and (d) 60 μm deep. (e) Zoomed-in section of (a) denoted by white box. (f) 2D maximum intensity Z-projection of the entire image stack with 20 μm between successive frames. (g) 3D reconstruction of image stack. Scale bars: (a)–(d), (f) 200 μm, (e) 100 μm.

image, and the three dimensional reconstruction is shown in Fig. 2(g) for comparison. Due to tissue absorption and scattering, the maximum imaging depth in colon tissue stained with acridine orange is approximately 60 μm.

Images were cropped to 1×42 mm^2 to more easily visualize tissue features along the length of the colons, and 1×2 mm^2 regions were selected and cropped to zoom in on the diverse crypt features in the colon tissue. Additionally, the images were resized to correct for non-square pixels. While the vertical pixel size is 1 μm, the horizontal pixel size is 0.78 μm when the stage is scanning at maximum speed. The images were skewed to achieve 1 μm^2 pixel size. The image contrast was enhanced and normalized for improved print viewing. To better illustrate the size of the extended FOV images and for comparison of crypt features in normal and inflamed colons, the Z-projection images of normal and inflamed tissue were combined in a video file (Video 1). Adobe Premiere Pro CS5 software was used to generate the video.

3 Results

Figure 3(a) shows 1×42 mm^2 of a Z-projection extended FOV image of normal mouse colon. The image is oriented with the proximal end, or ascending colon, to the left and the distal end, or sigmoid colon, to the right. Sample regions of interest from the length of the colon were selected, cropped to 1×2 mm^2, and enlarged to more clearly show cellular and crypt features in the image. These regions are depicted by white rectangles in Fig. 3(a). Figures 3(b) and 3(c) are cropped regions of Fig. 3(a) from the proximal region of the mouse colon. Figure 3(d) is a 5× microscope image of a histology slide prepared from a section of tissue at the proximal end of the colon. In the histological process, the tissue was oriented parallel to the mucosal surface such that the histology image would emulate the *en face* confocal image, to provide a direct comparison to confocal images. Similarly, confocal and histology images are shown for middle, Figs. 3(e)–3(g), and distal, Figs. 3(h)–3(j), regions of the colon. The 1×2 mm^2 confocal images and the 1×1.8 mm^2 histology images are shown on the same scale to enable comparison of crypt features. The extended FOV confocal image [Fig. 3(a)] is $1000 \times 42,000$ pixels. Figures 3(b), 3(c), 3(e), 3(f), 3(h), and 3(i) are 1000×2000 pixels.

The crypts shown in the confocal images of normal colon are uniform in size and distribution along the length of the colon, Fig. 3(b), 3(c), 3(e), 3(f), 3(h), and 3(i). The lumen size within the histology images, Fig. 3(d), 3(g), and 3(j), correlate with the confocal images and confirm the homogeneity of the colon. There is not a significant change in lumen size, shape, or distribution along the mouse colon tissue surface.

Figure 4(a) is a $1 \times 42 -$ mm^2 section of a Z-projection extended FOV image of chronic inflammation in the mouse colon. The white rectangles indicate the positions of Figs. 4(b) and 4(c) in the proximal region, Figs.4(e) and 4(f) in the middle region, and Fig. 4(h) and 4(i) in the distal region, moving left to right in the image. Figures 4(d), 4(g), and 4(j) are the corresponding *en face* histology images from the proximal, middle, and distal regions, respectively. The 1×2 mm^2 image locations were selected to highlight the diversity of tissue structure along the length of the inflamed colon.

In some areas within the confocal images of inflamed colon, the crypts appear uniform in size and shape, for example in Figs. 4(b), 4(c), and parts of 4(f). While in other locations, such as Figs. 4(e), parts of 4(f), 4(h), and 4(i), the crypts are spaced further apart or exhibit large lumen that are not circular in shape. As compared to the normal mouse colon, the inflamed tissue has a loss of architecture with non-uniform crypts that are
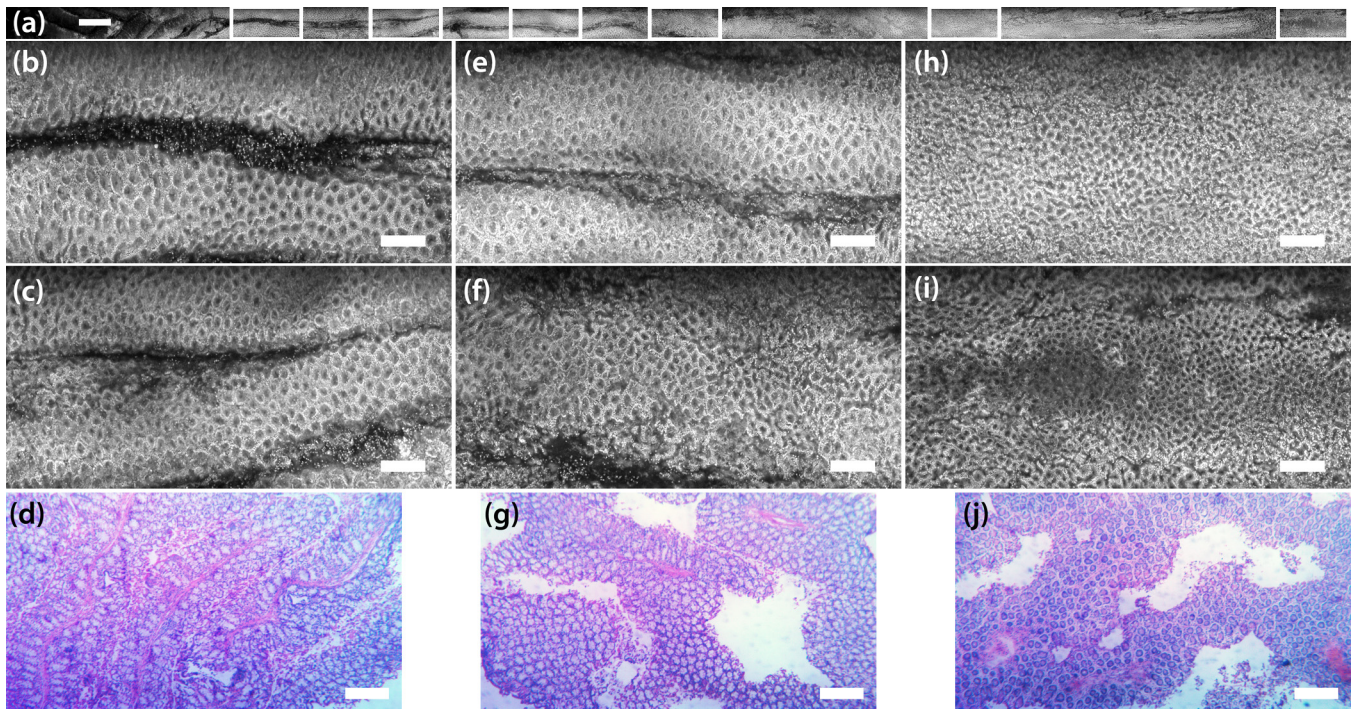
Fig. 3 Extended confocal microscopy and histology images of normal mouse colon. (a) 1×42 mm^2 Z-projection (Video 1, MPG4, 7.42 MB). Proximal side of colon is on the left. Scale bar: 1 mm. Figures 3(b), 3(c), 3(e), 3(f), 3(h), and 3(i) are sequential regions, 1×2 mm^2, of (a) designated by white boxes, from proximal [(b) and (c)], middle [(e) and (f)], and distal [(h) and (i)] regions. Scale bars: 200 μm. Figures 3(d), 3(g), and 3(j) are histology images, 1×1.8 mm^2, from proximal, middle, and distal regions, respectively. Scale bar: 200 μm. [URL: http://dx.doi.org/10.1117/1.JBO.17.1.016006.1]
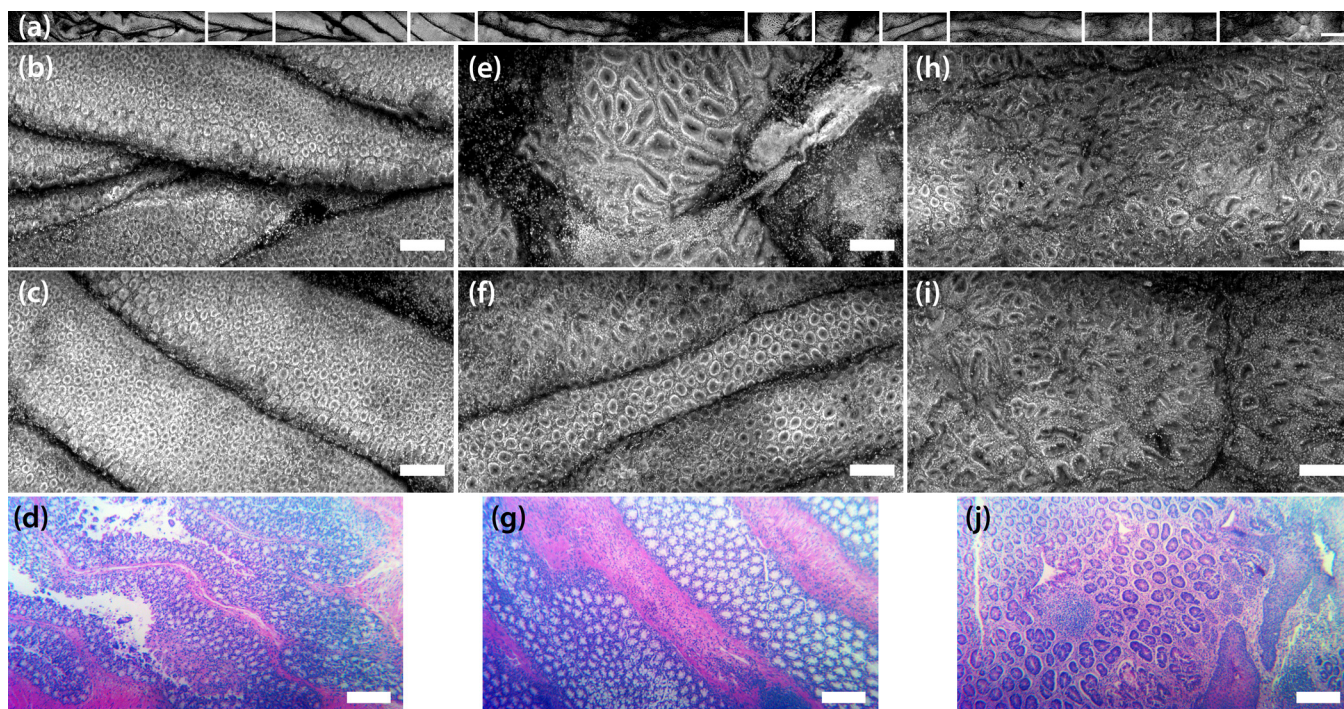
Fig. 4 Extended confocal microscopy and histology images of mouse colon with chronic inflammation. (a) 1×42 mm² Z-projection (Video 1, MPG4, 7.42 MB). Proximal side of colon is on the left. Scale bar: 1 mm. Figures 4(b), 4(c), 4(e), 4(f), 4(h), and 4(i) are sequential regions, 1×2 mm², of (a) designated by white boxes from proximal [(b) and (c)], middle [(e) and (f)], and distal [(h) and (i)] locations of mouse colon. Scale bars: 200 μm. Figures 4(d), 4(g), and 4(j) are histology images, 1×1.8 mm², from proximal, middle, and distal regions, respectively. Scale bar: 200 μm. [URL: http://dx.doi.org/10.1117/1.JBO.17.1.016006.1]

not evenly distributed across the tissue surface. The histology images of the mouse colon tissue with chronic inflammation show heterogeneity of the tissue as the lumen size varies from one location to another, Figs. 4(d), 4(g), and 4(j).

4 Discussion

We have constructed a confocal microscope combining beam scanning and rapid stage scanning at 7 mm/sec to rapidly acquire-high aspect ratio images. We demonstrate this technique on excised mouse colon to enable evaluation of tissue features along the length of the colon. Extended FOV images of normal mouse colon show the homogeneous distribution of colon crypts along the entire length of the colon. In contrast, the extended FOV images of inflamed tissue show a wide range of crypt size, shape, and distribution. Some regions appear quite normal; whereas, other regions show extremely distorted crypt structure. For example, if we compare the confocal image with the most severe crypt distortion in the inflamed colon [Fig. 4(e)] to an image taken near the same location in the normal colon [Fig. 3(f)], the average area and standard deviation of the crypts defined by the bright ring of colonocyte nuclei is 4231 ± 2226 μm² for the inflamed tissue and 1076 ± 332 μm² for the normal tissue. Furthermore, the average eccentricity and standard deviation decreases from 0.80 ± 0.14 to 0.73 ± 0.13 from inflamed to normal tissue, where a circle has an eccentricity of 0 and a line has an eccentricity of 1. Rapid confocal imaging and image processing could provide a quantitative map of crypt area and eccentricity to measure severity of tissue distortion with inflammation. It may also be used for fast identification of focal changes such as aberrant crypt foci, which are small groups of crypts with altered size and shape thought to be precursor lesions to colon cancer.[32]

Our current system configuration is intended for pre-clinical studies of excised mouse colon tissue. This technique can be further expanded to other applications by stitching multiple extended FOV images together to create a large-area image.[26] Potential clinical applications include dermatological[33] and gastroesophageal[27] studies. Combined beam and stage scanning could also increase the large field of view image acquisition speed for other point scanning microscopy techniques, such as non-linear microscopy. In comparison to other systems, the length of our images and speed of acquisition are significantly higher. The image acquisition speed is currently limited by the maximum speed of the translation stage. Use of a faster stage would further increase image acquisition speed to the point that the polygon scanning mirror, our fast axis line scanner, would be the limiting factor. The acquisition of image stacks is currently limited by data transfer and saving, and not limited by the translation stage.

We have presented confocal images that show potential for classifying an inflammatory region within the colon based on crypt lumen size, shape, and distribution. The homogeneity of normal mouse colon tissue compared to the heterogeneous nature of tissue exhibiting chronic inflammation is clearly evident within regions of the colon. Some regions within the inflamed colon, Figs. 4(b) and 4(c) for example, may be considered "normal;" therefore, a rapid stage-scanning image technique to evaluate the entire organ to identify regions of interest may be valuable. We are able to acquire data along the entire length of the mouse colon in a relatively short period of time.

References

1. E. V. Loftus, Jr., "The burden of inflammatory bowel disease in the United States: a moving target?," *Clin. Gastroenterol. Hepatol* **5**(12), 1383–1384 (2007).

2. W. Strober, I. Fuss, and P. Mannon, "The fundamental basis of inflammatory bowel disease," *J Clin Invest* **117**(3), 514–521 (2007).

3. American Cancer Society, "*Colorectal Cancer Facts & Figures 2008–2010*," American Cancer Society, Atlanta (2008).

4. D. K. Podolsky, "Inflammatory bowel disease," *N. Engl. J. Med.* **347**(6), 417–429 (2002).

5. S. H. Itzkowitz and X. Y. Yio, "Inflammation and cancer—IV. Colorectal cancer in inflammatory bowel disease: the role of inflammation," *Am. J. Physiol. Gastrointest. Liver Physiol.* **287**(1), G7–G17 (2004).

6. B. Levin et al., "Screening and surveillance for the early detection of colorectal cancer and adenomatous polyps, 2008: a joint guideline from the American Cancer Society, the US Multi-Society Task Force on Colorectal Cancer, and the American College of Radiology," *Gastroenterology* **134**(5), 1570–1595 (2008).

7. S. C. Larsson and A. Wolk, "Meat consumption and risk of colorectal cancer: a meta-analysis of prospective studies," *Int. J. Cancer* **119**(11), 2657–2664 (2006).

8. A. Chao et al., "Meat consumption and risk of colorectal cancer," *JAMA* **293**(2), 172–182 (2005).

9. Q. Jia et al., "Reduced colitis-associated colon cancer in fat-1 (n-3 fatty acid desaturase) transgenic mice," *Cancer Res.* **68**(10), 3985–3991 (2008).

10. R. S. Chapkin et al., "Mechanisms by which docosahexaenoic acid and related fatty acids reduce colon cancer risk and inflammatory disorders of the intestine," *Chem. Phys. Lipids* **153**(1), 14–23 (2008).

11. R. S. Chapkin, D. N. McMurray, and J. R. Lupton, "Colon cancer, fatty acids and anti-inflammatory compounds," *Curr. Opin. Gastroenterol.* **23**(1), 48–54 (2007).

12. D. S. Levine and R. C. Haggitt, "Normal histology of the colon," *Am. J. Surg. Pathol.* **13**(11), 966–984 (1989).

13. J. T. C. Liu et al., "Dual-axes confocal reflectance microscope for distinguishing colonic neoplasia," *J. Biomed. Opt.* **11**(5), 054019 (2006).

14. O. Watanabe et al., "Confocal endomicroscopy in patients with ulcerative colitis," *J. Gastroenterol. Hepatol.* **23**, S286–S290 (2008).

15. C. M. Park et al., "A simple, practical 'swiss roll' method of preparing tissues for paraffin or methacrylate embedding," *J. Microsc.* **145**, 115–120 (1987).

16. J. B. Pawley, *Handbook of Biological Confocal Microscopy*, Springer, New York, NY (2006).

17. W. B. Amos and J. G. White, "How the confocal laser scanning microscope entered biological research," *Biol. Cell* **95**(6), 335–342 (2003).

18. A. Hoffman et al., "Confocal laser endomicroscopy: technical status and current indications," *Endoscopy* **38**(12), 1275–1283 (2006).

19. M. Minsky, "Memoir on inventing the confocal scanning microscope," *Scanning* **10**, 128–138 (1988).

20. C. J. R. Sheppard, "15 years of scanning optical microscopy at Oxford," *SPIE Milestone Series MS* **131**, 18–21 (1996).

21. P. Davidovits and M. D. Egger, "Scanning laser microscope," *Nature* **223**(5208), 831 (1969).

22. G. J. Brakenhoff, P. Blom, and P. Barends, "Confocal scanning light-microscopy with high aperture immersion lenses," *J. Microsc-Oxford* **117** 219–232 (1979).

23. J. G. White, W. B. Amos, and M. Fordham, "An evaluation of confocal versus conventional imaging of biological structures by fluorescence light microscopy," *J. Cell Biol.* **105**(1), 41–48 (1987).

24. A. L. Carlson et al., "Dual-mode reflectance and fluorescence near-video-rate confocal microscope for architectural, morphological and molecular imaging of tissue," *J. Microsc.* **228**(Pt 1), 11–24 (2007).

25. Y. G. Patel et al., "Confocal reflectance mosaicing of basal cell carcinomas in mohs surgical skin excisions," *J. Biomed. Opt.* **12**(3), 034027 (2007).

26. S. Abeytunge et al., "Rapid confocal imaging of large areas of excised tissue with strip mosaicing," *J. Biomed. Opt.* **16**(5), 050504 (2011).

27. D. Kang et al., "Comprehensive imaging of gastroesophageal biopsy samples by spectrally encoded confocal microscopy," *Gastrointest. Endosc.* **71**(1), 35–43 (2010).

28. P. Kim et al., "In vivo wide-area cellular imaging by side-view endomicroscopy," *Nat. Methods* **7**(4), 303–305 (2010).

29. T. Wilson, "Optical sectioning in confocal fluorescent microscopes," *J. Microsc-Oxford* **154**(2), 143–156 (1989).

30. H. S. Cooper et al., "Clinicopathologic study of dextran sulfate sodium experimental murine colitis," *Lab Invest* **69**(2), 238–249 (1993).

31. T. Tanaka et al., "A novel inflammation-related mouse colon carcinogenesis model induced by azoxymethane and dextran sodium sulfate," *Cancer Sci.* **94**(11), 965–973 (2003).

32. E. A. Mclellan, A. Medline, and R. P. Bird, "Dose-response and proliferative characteristics of aberrant crypt foci: putative preneoplastic lesions in rat colon," *Carcinogenesis* **12**(11), 2093–2098 (1991).

33. D. S. Gareau et al., "Confocal mosaicing microscopy in skin excisions: a demonstration of rapid surgical pathology," *J. Microsc-Oxford* **233**(1), 149–159 (2009).